A Detailed Comparison on the Influence of Flow Unsteadiness Between the Vaned and Vaneless Mixed-Flow Turbocharger Turbine

M. H. Padzillah
UTM Centre for Low Carbon Transport in Cooperation,
Imperial College London,
Universiti Teknologi Malaysia,
Johor Bharu 81310, Malaysia
e-mail: mhasbullah@utm.my

S. Rajoo
UTM Centre for Low Carbon Transport in Cooperation,
Imperial College London,
Universiti Teknologi Malaysia,
Johor Bharu 81310, Malaysia

R. F. Martinez-Botas
Department of Mechanical Engineering,
Imperial College London,
Exhibition Road,
London SW7 2AZ, UK

A turbocharger is a key enabler for lowering CO_2 emission of an internal combustion engine (ICE) through the reutilization of the exhaust gas energy that would otherwise have been released to the ambient. In its actual operating conditions, a turbocharger turbine operates under highly pulsating flow due to the reciprocating nature of the ICE. Despite this, the turbocharger turbines are still designed using the standard steady-state approach due to the lack of understanding of the complex unsteady pressure and mass propagation within the stage. The application of guide vanes in a turbocharger turbine stage has increased the complexity of flow interactions regardless of whether the vanes are fixed or variable. Although it is enticing to assume that the performance of the vaned turbine is better than the one without (vaneless), there are currently no tangible evidences to support this claim, particularly during the actual pulsating flow operations. Therefore, this research looks into comparing the differences between the two turbine arrangements in terms of their performance at flow field level. For this purpose, a three-dimensional (3D) "full-stage" unsteady turbine computational fluid dynamics (CFD) models for both volutes are constructed and validated against the experimental data. These models are subject to identical instantaneous inlet pressure profile of 60 Hz, which is equivalent to an actual three-cylinder four-stroke engine rotating at 2400 rpm. A similar 95.14 mm diameter mixed-flow turbine rotor rotating at 48,000 rpm is used for both models to enable direct comparison. The complete validation exercises for both steady and unsteady flow conditions are also presented. Results have indicated that neither vaned nor vaneless turbine is capable of maintaining constant efficiency throughout the pulse cycle. Despite that, the vaneless turbine indicated better performance during peak power instances. This work also showed that the pulsating pressure at the turbine inlet affected the vaned and vaneless turbines differently at the flow field level. Furthermore, results also indicated that both the turbines matched its optimum incidence angle for only a fraction of pulse cycle, which is unfavorable. [DOI: 10.1115/1.4038076]

Keywords: pulsating flow, mixed-flow turbine, computational fluid dynamics, turbocharger

1 Introduction

Conventional internal combustion engine (ICE) in automotive industry waste about 60% of the energy contained in liquid fuel to the ambient atmosphere in terms of heat. Not only that this issue has resulted in high fuel consumptions, it also leads to elevated level of greenhouse gas emission. With the estimated number of vehicle in excess of 1 billion in 2010 and increasing, waste heat from ICE is ultimately capable of influencing climate change at global level. One of the technologies to harness this waste heat is turbocharger. In automotive vehicles, turbocharger is usually installed close to the exhaust valve to maximize its potential to extract energy. In turn, the turbocharger turbine is exposed to highly pulsating flow due to reciprocating nature of ICE. It is essential for the turbocharger to match properly with the engine capacity in order to be able to operate reliably. To compensate for low flow rate, guide vane is usually installed to accelerate the flow before impacting turbine rotor. It could also be used to regulate the flow angle for the purpose of increasing the turbine efficiency.

In an ideal steady flow conditions, a novel study by Baines and Lavy [1] indicated that vaned turbine results in higher peak efficiency at a design point as compared to its vaneless counterpart. However, as the operating conditions move away toward off-design conditions, vaned turbine is not capable of maintaining its high efficiency. Meanwhile, even though the vaneless turbine does not have as high maximum efficiency as the vaned turbine, it is capable of maintaining relatively flat efficiency curve throughout the entire operation range. This means that at off-design conditions, the vaneless turbine could harness the waste heat better than the vaned turbine. However, the finding by Baines and Lavy [1] seems to have contradicted a more recent investigation by Spence et al. A comprehensive research by Spence et al. [2] has pointed that the vaneless turbine always indicates higher efficiency than vaned turbine. Although both works show contradicting results between each other, the initial setup that specified the working fluid as steady state is not representative of actual

Contributed by the Turbomachinery Committee of ASME for publication in the Journal of Engineering for Gas Turbines and Power. Manuscript received February 15, 2017; final manuscript received August 1, 2017; published online October 31, 2017. Assoc. Editor: Riccardo Da Soghe.

pulsating flow conditions. The ideal conditions can only serve as a reference since in pulsating flow conditions, the turbine operates most of the time at off-design conditions [3].

The use of experimental approach in investigating pulsating flow performance of a turbocharger turbine is prohibitively expensive for detailed flow analysis within the turbine stage. Therefore, the instantaneous flow data obtained are best used as validation parameters for numerical models. Yang et al. [4] conducted experimental work to directly compare pulsating flow performance between vaned and vaneless turbine under pulsating flow conditions. In the research, Yang et al. [4] indicated that the performance of turbocharger turbine under pulsating flow conditions is highly associated with the pulse frequency and loading (amplitude). They also concluded that vaned turbine is superior at low loading conditions as compared with its vaneless counterpart. Furthermore, they also indicated that the peak performance under steady flow condition is almost similar to each other. This is yet another contradicting result between researchers. Although Yang et al. [4] have conducted extensive testing at multiple flow frequencies and turbine loadings, the profile instantaneous pressure at the turbine inlet cannot be easily controlled. This could potentially invalidate the comparison of different turbine configuration even though it is operating at similar speed and loading. This disadvantage could be overcome by the means of computational simulation. Computational fluid dynamics (CFD) is an extensive tool for solving continuity, momentum, and energy conservation equations. This capability, coupled with the existence of experimental data for validation, could be particularly useful for investigating the flow field in greater details.

Simulation of turbocharger turbine operating under pulsating flow conditions was first attempted by Lam et al. [5]. This is to measure the capability of CFD to capture pulsating flow behavior of the turbocharger turbine. Lam et al. [5] used the "frozen rotor" approach where there are no relative motions between stationary (volute) and rotating (rotor) domain during the simulation, and the information on rotational speed of the rotor is integrated directly into the source term. Lam indicated that the use of frozen rotor method is valid for steady flow condition and that the use for this method for unsteady simulation is only valid when the frequency of the pulse is much smaller than that of the rotor frequency. In this work, Lam used the pulse frequency of 53.33 Hz and the turbine frequency of 2267 Hz. Lam also had difficulties in obtaining accurate quantitative results due to difficulties in getting the simulation to converge. Instead, qualitative results were presented. Despite that, this work has proven that it is possible to capture the influence of pulsating flow within the turbocharger turbine stage.

Palfreyman and Martinez-Botas [6] improved the work of Lam by using sliding interface between stationary and rotating domain. This allows relative motion between the volute and rotor during the simulations. This model is then validated with the work of Karamanis et al. [7] that utilized laser Doppler velocimetry measurement to investigate change in flow angle during a single pulse cycle. The work of Palfreyman and Martinez-Botas [6] has again shown that CFD is sufficient in capturing pulsating flow behavior in a turbine stage. This work also compares the flow field between radial and mixed flow turbine. They later indicated that the mixed flow turbines have a slight advantage over their radial counterparts attributed to smaller region of entropy generation close to tip near suction surface. This occurs since the degree of turning required using mixed flow turbine is less than the radial turbine. Recent work by Copeland et al. [8] and Newton et al. [9] also shows that CFD is a useful tool in investigating how the turbocharger turbine performs under pulsating flow conditions. Newton et al. [9] introduced the concept of "Lambda parameter" in determining level of "unsteadiness" of the turbine based on the residence time of a particular particle in each domain. This is representative of mass imbalance, which is the ratio between time-averaged mass flow changes in the domain and time-averaged mass flow through the domain [10]. Newton et al. [9] concluded that the turbine unsteadiness does not only depend on the flow frequency but also its amplitude.

Padzillah et al. [11] attempted to utilize this method and has successfully compared the flow angle behavior for both vaned and vaneless volute arrangement at a single pulsating flow operation. Padzillah et al. [11] concluded that nozzleless volute is more sensitive toward changes in instantaneous pressure as compared to vaned volute. However, as this work is the first one attempted to directly compare vaned and vaneless volute under pulsating flow, Padzillah et al. [11] used the boundary conditions provided by Yang et al. [4], thus still maintaining different instantaneous pressure profile at the turbine inlet.

In order to enable direct comparison of performance and flow field behavior, the use of similar pressure profile at the inlet is necessary. Therefore, this research intends to compare the effect of pulsating flow operation between vaned and vaneless volute in terms of its performance and the flow field behavior using identical inlet time-dependent boundary conditions. The analysis particularly on the static pressure and flow angle distributions, which are critical to the overall performance of the turbine, is investigated in great details by means of validated CFD technique. To the best of authors' knowledge, such work has yet to be attempted, thus highlighting the novelty of the current work.

2 Methodology

In achieving the aims of the current work, both experimental and numerical works are conducted. The purpose of experimental work is mainly to obtain validation data as well as the boundary conditions for numerical work. For instance, the information with regard to the pressure as well as temperature profile in relation with time is required during simulation, and this could only be obtained through experiments.

2.1 Experimental Methodology. The experimental work was conducted at the turbocharger test facility in Imperial College London. This includes both steady and unsteady measurements for vaned and vaneless turbines. For the unsteady flow condition, a flow frequency of 60 Hz, which is equivalent to 2400 rpm single entry three-cylinder four-stroke engine, was chosen. The "similarity approach" developed by Glassman in 1972 was used to calculate equivalent mass flow parameter (MFP) and the turbine rotational speed, given the cold flow nature of the test facility. The equivalent conditions are described in the following equations:

$$\left(\frac{\dot{m}\sqrt{T_{01}}}{P_{01}}\right)_{\text{test-rig}} = \left(\frac{\dot{m}\sqrt{T_{01}}}{P_{01}}\right)_{\text{actual}} \tag{1}$$

$$\left(\frac{N}{\sqrt{T_{01}}}\right)_{\text{test-rig}} = \left(\frac{N}{\sqrt{T_{01}}}\right)_{\text{actual}} \tag{2}$$

The three-dimensional (3D) representation of the cold-flow turbocharger test facility is shown in Fig. 1. Three screw-type compressors that are capable of supplying air up to 1 kg/s at 5 bars feed the air into the test rig. Downstream the air inlet is the safety and control valve that is regulated from the control room located next to the test rig. Two heaters are used to increase the air temperature in order to avoid condensation due to air expansion in the turbine. The air temperature is kept between 60 °C and 65 °C during testing. The flow is then channeled into two 81.4 mm limbs, namely inner and outer limb, based on their relative positions. This allows testing for multiple entry turbines. For the current single entry test, the two limbs are merged just before the turbine inlet by a slightly tapered duct. Downstream the heaters, for steady flow testing, the mass flow rate for the individual limbs is measured by orifice plate as well as the v-cone flow meter. The flow will then flow through the pulse generator that consists of rotating chopper

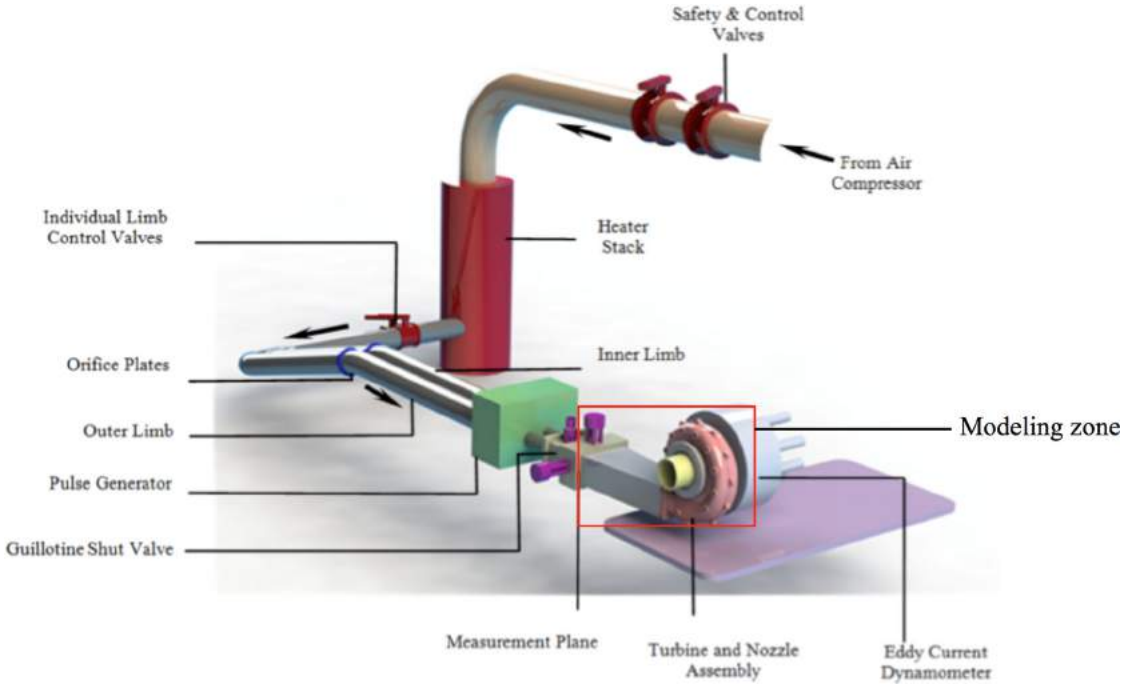

Fig. 1 The schematic of the cold-flow turbocharger test facility in Imperial College London

plates originally developed by Dale and Watson [12]. The plate is designed to replicate the actual pulse from the exhaust valve on an engine where its rotation is electronically controlled to provide the desired flow frequency. The electric motor-driven pulse generator could generate up to 80 Hz pulse flow frequency and could be adjusted to operate in-phase or out-of-phase. Meanwhile, for steady-state flow, the chopper plates are simply locked to their fully open position to allow maximum air flow. Furthermore, almost all unsteady parameters are measured at the measurement plane downstream the pulse generator. At this location, instantaneous pressure and mass flow rate, as well as mean temperature, are measured.

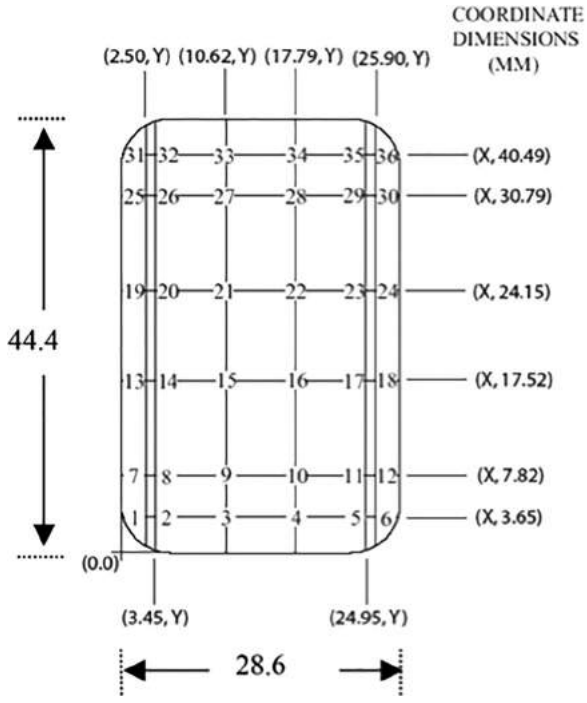

Fig. 2 The 36 grid hotwire measurement location in the flow duct [13]

Perhaps, one of the most challenging measurements in the current work is the measurement on instantaneous mass flow rate. For this purpose, a traversing system for a 10 μm platinum-plated tungsten constant-temperature hotwire anemometer was utilized to obtain the mass flux throughout the cross section of the measurement plane. A total number of 36 points was selected, with decreasing grid size close to the wall, as shown in Fig. 2. As the temperature fluctuates heavily during measurement, two-stage calibration procedures are needed. For the first stage, the hotwire is calibrated at room temperature of 24 °C in order to fit the calibration curve of King's Law. The second stage calibration was conducted after the hotwire has been attached to the traversing mechanism. The 36 point readings are integrated in accordance to British standard BS1042, 1983. The values are then multiplied with the duct area at measurement plane to obtain the mass flow rate. During the measurement, the hotwire system was set up to run on constant over-heat ratio during both calibration process and the actual testing, which involves two different temperatures. Therefore, the measured raw data were corrected for temperature. Effects of properties such as Prandtl number (Pr), thermal conductivity (k), dynamic viscosity, density, and the Mach number are taken into account when amending the calibration factor during unsteady testing.

Downstream the measurement plane, the turbine is attached to an eddy current dynamometer through a common shaft. Figures 3 and 4 show the components of the turbine used in the current work as well as the arrangements of vaneless and vaned volute, respectively. The permanent magnet at the end of the shaft is located closely with two stators at both ends. The distance between magnet and stator is controlled by servo motors for the purpose of adjusting power absorption capacity of the dynamometer. The maximum power absorption for this dynamometer is 60 kW. The two stators are heavily cooled by a separated water cooling system to remove the extensive heat from the stator plates, as shown in Fig. 5. The assembly of the dynamometer is free to rotate on a gimbal bearing to allow direct torque measurement using a connecting arm and a load cell. A high-speed optical

Fig. 3 Components of the turbine stage that include the volute, pivoting mechanism, lean vanes and adjustment ring

Fig. 4 Experimental setup that shows (*a*) vaneless turbine and (*b*) vaned turbine

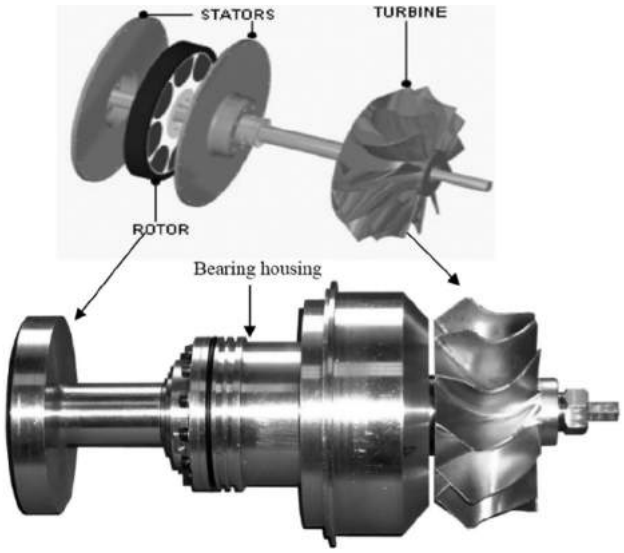

Fig. 5 Main components of the eddy current dynamometer [14]

sensor is also installed within the dynamometer assembly for turbine speed measurement. Moreover, the current arrangement of the test rig also allows for additional equipment to be installed between the turbine and dynamometer assembly such as actuator system for Active Control Turbocharger developed by Pesiridis and Martinez-Botas [15]. The utilization of eddy current dynamometer has enabled the turbine to be tested at extended operating range. At current capacity, the test rig is able to measure performance range up to 300% wider than that provided by the manufacturer. Not only this capability helps in unsteady flow measurement, it also helps in predicting off-design condition of the turbine [16]. There are also multiple high-speed pressure sensors installed across the periphery of the volute for further analysis as well as to assist model validations in the later stage of the work. The elaborated details on the test rig setup and procedures are well documented in Ref. [13].

2.2 Numerical Methodology. In order to enable detailed flow field analysis of the two types of stator arrangement, a full-stage 3D CFD was built. The model consists of four components, which are the inlet duct, turbine volute, the vanes, and turbine wheel. The geometrical configuration for both vaned and vaneless turbine was derived from the exact dimension of the actual components tested in the experimental work explained in Sec. 2.1. The connecting duct was modeled by taking the measurement plane as the duct inlet and the volute entry as its outlet. The volute design was based on a modified Holset H3B with the intended exit flow angle of 69 deg [13]. These two components (inlet duct and volute) were modeled in SOLIDWORKS, where the meshing process subsequently took place using ICEM CFD package. This package enables the complete control of the hexahedral mesh placement, which is crucial in meshing the complex geometry such as the volute.

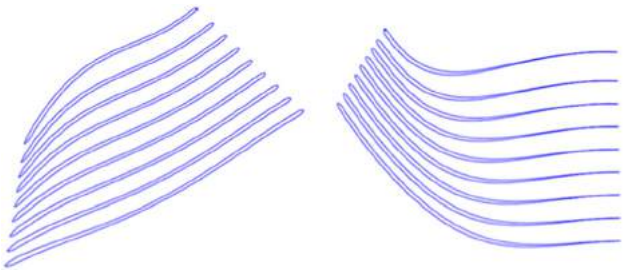

Fig. 6 The generated profile lines for Rotor A

Table 1 Geometrical details of the turbine

Geometrical Feature	Dimension
Leading edge tip diameter (mm)	95.14
Leading edge span height (mm)	18.00
Trailing edge tip diameter (mm)	78.65
Trailing edge span height (mm)	25.79
Cone angle (deg)	40.00
Leading edge blade angle (deg)	20.00
Root-mean-radius at trailing edge (mm)	52.00
Length of axial chord (mm)	40.00
Number of blades	12
Tip gap height (% of blade span)	3.00

Table 2 Node distribution in the computational domain

Domain	Number of nodes	Type of mesh
Inlet duct	242,320	Unstructured hexahedral
Volute	730,016	Unstructured hexahedral
Nozzle	590,160	Structured hexahedral
Rotor	2,600,436	Structured hexahedral
Total	4,162,932	

For the vaned turbine arrangement, the vane blades were created using Bezier Polynomials in order to generate five profile lines starting with the hub until shroud. The vanes that are utilized for the simulation are based on NACA 0015 profile with the lean geometry of 50 deg from the hub surface [13]. The vanes consist of 15 blades with different chord length of 22.3 mm and 26.3 mm for hub and shroud, respectively. The clearance gap that exists between hub and shroud wall to the blade was measured instead of relying on its intended clearance gap. Padzillah et al. in their previous work proved that this step is necessary in order to prevent underprediction of the static pressure at the blade surfaces [17]. The turbine wheel profiles were generated using similar approach as the vanes. However, nine profile lines were generated instead of five due to additional geometrical complexity of the rotor instead of the vanes as shown in Fig. 6. Geometrical details of the research turbine wheel, designated "Rotor A," are tabulated in Table 1.

Subsequently, both the vane and the rotor wheel are meshed using TURBOGRID package. The package requires profile lines, as well as hub and shroud coordinates, in order to create structured hexahedral mesh elements. The inlet and outlet of the domain are controlled using hub and shroud control points. For vaned turbine arrangement, the inlet of the rotor corresponds directly to the vane exit. However, for vaneless arrangement, the inlet of the rotor is extended to the volute exit.

The meshed geometries are then exported to ANSYS CFX PRE for assembly. At this stage, the interfaces between the components, as well as the boundary conditions, are specified. For the interface between stationary components such as volute and vane, general interface is selected. However, for the interface between stationary and rotating components, i.e., between volute and rotor for vaneless configuration (and between vane and rotor for vaned configuration), a "transient" interface was specified. This enables relative movement between stationary and rotating domain as the time-step advances in the simulation. Therefore, the selection of time-step becomes critical. For the current work, the selected transient time-step is 3.472×10^{-6} s, which is equivalent to 1 deg of turbine rotation. In unsteady flow simulation, a transient interface is preferable as compared to the frozen rotor, which prevents the rotating domain to move [6], albeit at the expense of extended computational time. For the spatial discretization, a mesh independence test was conducted in advanced to acquire minimum number of nodes for stable solution. The final selection of node counts for each of the components is tabulated in Table 2.

Following the interface setup is the definition of boundary conditions. At the domain inlet shown in Fig. 7, the time-dependent total pressure and temperature are specified. The pressure and temperature profile are based on the experimental data recorded at the measurement plane, which correspond to the inlet of the connecting duct in the numerical model. The direction of the flow is specified in such a way that the only velocity component that exists is normal to the inlet plane. At the domain outlet, a constant value of atmospheric pressure is applied. For both vaned and vaneless turbine configurations, similar inlet and outlet boundary conditions are specified to enable direct comparison of performance and flow field analysis. Furthermore, a no-slip boundary condition was specified at all walls including the vanes and rotor blades.

With regard to the rotational speed of the turbine wheel, the maximum speed fluctuation recorded during experimental work is only within ±1.5% of the cycle-averaged value. As CFX does not provide options for specifying time-dependent rotational speed, a constant speed of 48,000 rpm is justified. Steady-state simulation was conducted prior to the unsteady simulation in order to obtain the initial file. This would help convergence in the calculation of

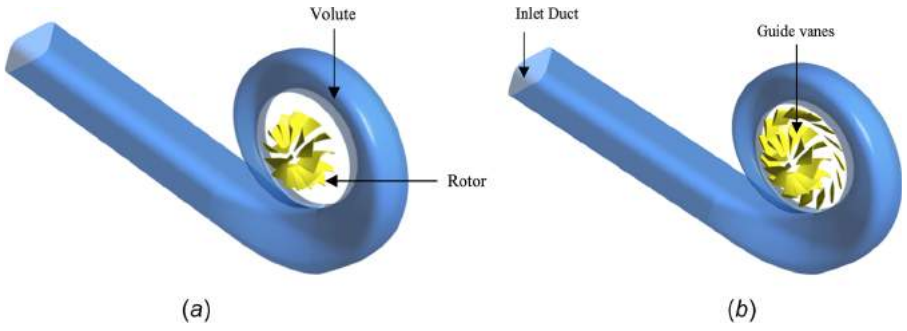

Fig. 7 Assembly of the meshed geometries for (*a*) vaneless and (*b*) vaned

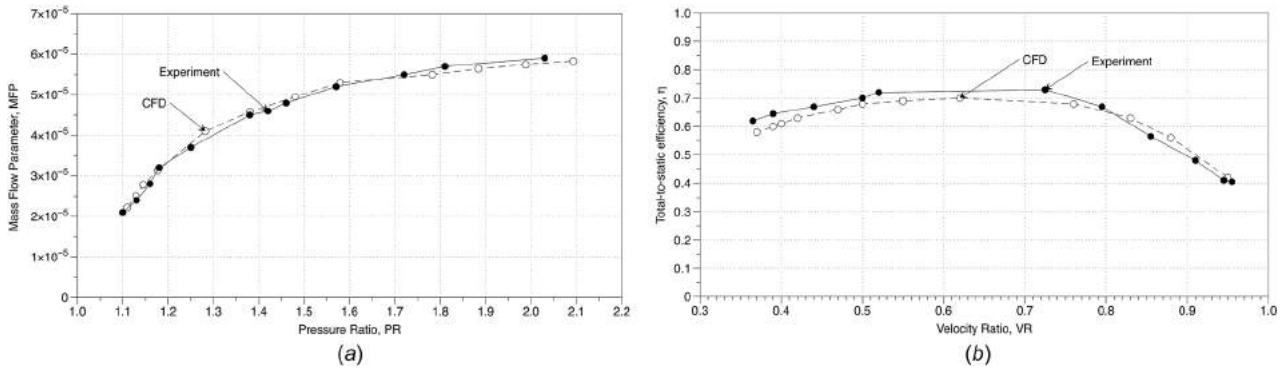

Fig. 8 Comparison between CFD and experimental data of (*a*) MFP against pressure ratio and (*b*) total-to-static efficiency against velocity ratio (VR) for vaned volute configuration

unsteady simulations. For each of the volute arrangements, a total number of three pulses were simulated to enable cycle convergence. Total computational time is recorded to be 21 days for each arrangement using high-performance computer facility in imperial college London with 8 cores and 2 Gb memory for each of the cores, resulting in excess of 2TB of the transient result files.

The calculations are made in ANSYS CFX solve package that implicitly solve for the unsteady Reynolds-averaged Navier–Stokes equation. The continuity and momentum equations are defined as

$$\frac{\partial \rho}{\partial t} + \frac{\partial (\rho U_i)}{\partial x_i} = 0 \tag{3}$$

As the flow is assumed as incompressible in the current model, the equation can be reduced to

$$\frac{\partial U_i}{\partial x_i} = 0 \tag{4}$$

Meanwhile, the Reynolds-averaged Navier–Stokes equation is defined as

$$\rho\left(\frac{\partial U_i}{\partial t} + U_j \frac{\partial U_i}{\partial x_j}\right) = \frac{\partial P}{\partial x_i} + \frac{\partial}{\partial x_j}\left(\mu \frac{\partial U_i}{\partial x_j} - \rho \overline{u_i' u_j'}\right) \tag{5}$$

The additional Reynolds stress term in Eq. (5) is solved by selection of the two-equation *k-epsilon* turbulence model. The particular model has been chosen for closure of Navier–Stokes equation due to its robustness, as well as its ability to correctly predict turbine performance when compared to experimental data. Subsequently, following the completion of numerical calculation, the results in the form of performance parameters as well as instantaneous mass flow rate are subject to validation process by comparing the predicted values with experimentally measured values.

3 Results and Discussion

This section discusses the two-stage validation procedures, followed by discussion on the key performance and flow field differences between the two volute arrangements.

3.1 Model Validations

3.1.1 Steady Flow Validations. Once the simulation is completed, the results are compared and validated against experimental results. As the unsteady simulation could take several weeks to complete, it is important to validate the steady-state simulations first before moving on to unsteady flow simulation. This allows optimization to the steady-state model to be made before committing to lengthy unsteady simulations. Validation of steady-state simulations is made by calculating the turbine performance parameter such as the pressure ratio (PR), velocity ratio, mass flow parameter, and total-to-static efficiency. The formula for obtaining the turbine performance parameters are shown in Eqs. (6)–(12)

$$\text{pressure ratio, PR} = \frac{P_{01}}{P_5} \tag{6}$$

$$\text{mass flow parameter, MFP} = \frac{\dot{m}\sqrt{T_{01}}}{P_{01}} \tag{7}$$

$$\text{total} - \text{to} - \text{static efficiency, } \eta = \frac{W_{\text{act}}}{W_{\text{isen}}} \tag{8}$$

$$\text{actual power, } W_{\text{act}} = 2 \cdot \pi \cdot N \cdot \tau \tag{9}$$

$$\text{isentropic power, } W_{\text{isen}} = \dot{m} \cdot c_p \cdot T_{01}\left[1 - \left(\frac{P_5}{P_{01}}\right)^{\frac{\gamma-1}{\gamma}}\right] \tag{10}$$

$$\text{velocity ratio, VR} = \frac{U}{C_{is}} \tag{11}$$

$$\text{isentropic velocity, } C_{is} = \sqrt{2 \cdot \frac{W_{\text{isen}}}{\dot{m}}} \tag{12}$$

Figure 8(*a*) shows the plot of mass flow parameter against pressure ratio for CFD and experimental data. It can be seen that the numerical calculation is able to capture not only the trend but also the magnitude of experimental mass flow parameter. The root-mean-square of the deviation over the entire simulation range is recorded to be 2%. Meanwhile, the total-to-static efficiency against velocity ratio for CFD and experiment is plotted in Fig. 8(*b*). Although it is expected that the CFD calculations would result in higher efficiency as some of the losses such as the back-face loss are not accounted; this is not the case for the current work. However, as the results of CFD are still well within the experimental uncertainty, the workability of the model is sound. The figures indicated that the steady-state simulation is capable of capturing the information regarding the turbocharger performance with sufficient accuracy across the entire operating range at the particular speed. This enables the use of similar model for unsteady flow simulation.

3.1.2 Pulsating Flow Validations. The validation procedure for unsteady flow simulation focuses on the measured parameters rather than its derivatives. This is done in order to directly detect if there exist any deviation that might contribute to errors in the calculation of the derivative performance parameters later. Therefore, the comparison with experimental data is done relative to the time domain. This step also ensures that the extracted parameters

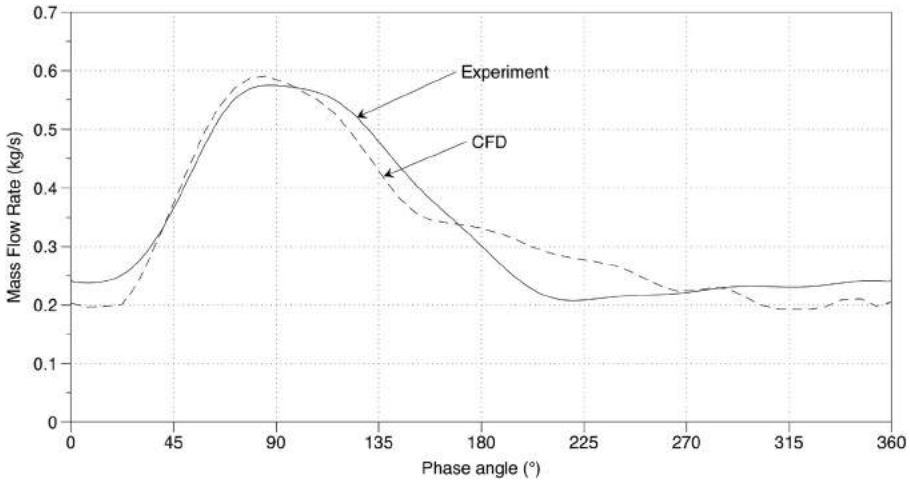

Fig. 9 Comparison of instantaneous mass flow rate between CFD and experimental data

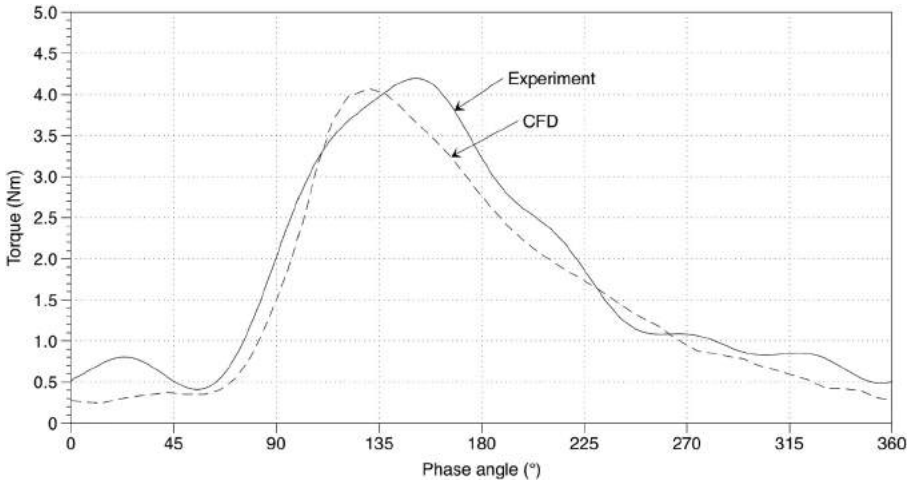

Fig. 10 Comparison of instantaneous torque between CFD and experimental data

are sufficient to capture the experimental trace over time. Moreover, it also ensures that the specified time-step is sufficiently small to capture the effect of unsteady phenomena within the turbine stage. Two of the most difficult parameters to obtain, namely instantaneous mass flow rate and instantaneous torque, were chosen as the validation parameters.

Figure 9 shows the plot of mass flow rate phase angle for both CFD and experimental measurements. The phase angle is representative of time where one complete 360 deg cycle is equivalent to a single pulse. It can be seen that the CFD model is able to predict the magnitude of range of mass flow rate sufficiently well. However, it seems to underpredict the mass flow rate right after the peak and then overpredict it between 170 deg and 270 deg phase angle. However, on average, CFD underpredicted the experimental mass flow rate by only 0.9%. This is a good indication that the numerical model is able to capture the pulsating flow behavior sufficiently well.

Figure 10 shows the plot of instantaneous rotor torque against the phase angle for both CFD and experimental measurement. In experimental work, the instantaneous torque is obtained by summing the mean torque value recorded by the load cell and the angular acceleration of the turbine wheel as shown in Eq. (13). This method of acquiring instantaneous torque is different from simulation where the instantaneous torque is calculated using Eq. (14).

$$\text{experimental total torque}, \tau(t)_{\text{exp}} = \overline{\tau} + I \cdot \frac{d\omega}{dt} \tag{13}$$

$$\text{simulation total torque}, \tau(t)_{\text{sim}} = \int \vec{r} \times (\vec{f}(t) \cdot \hat{n}) ds \tag{14}$$

Albeit different method is used, the plot of instantaneous torque in Fig. 10 shows almost exact agreement between experimental and computational. The magnitude is well predicted and the trend is well captured despite slight shift in phase angle at the peak. Time-averaged data indicated that CFD underpredicted the experimental value by a small 1.4%. Therefore, based on the steady-state validation as well as unsteady flow validation, it can be concluded that the developed model has achieved sufficient accuracy for further analysis.

3.2 Analysis of Results

3.2.1 Comparison of Incidence Flow Angle and Its Effect on Instantaneous Efficiency. Figure 11 shows the plot of instantaneous total-to-static efficiency against incidence angle at the rotor leading edge for vaned and vaneless turbine configurations. Circular markers indicated the instantaneous efficiency during pressure rise period while square marker indicated the turbine efficiency

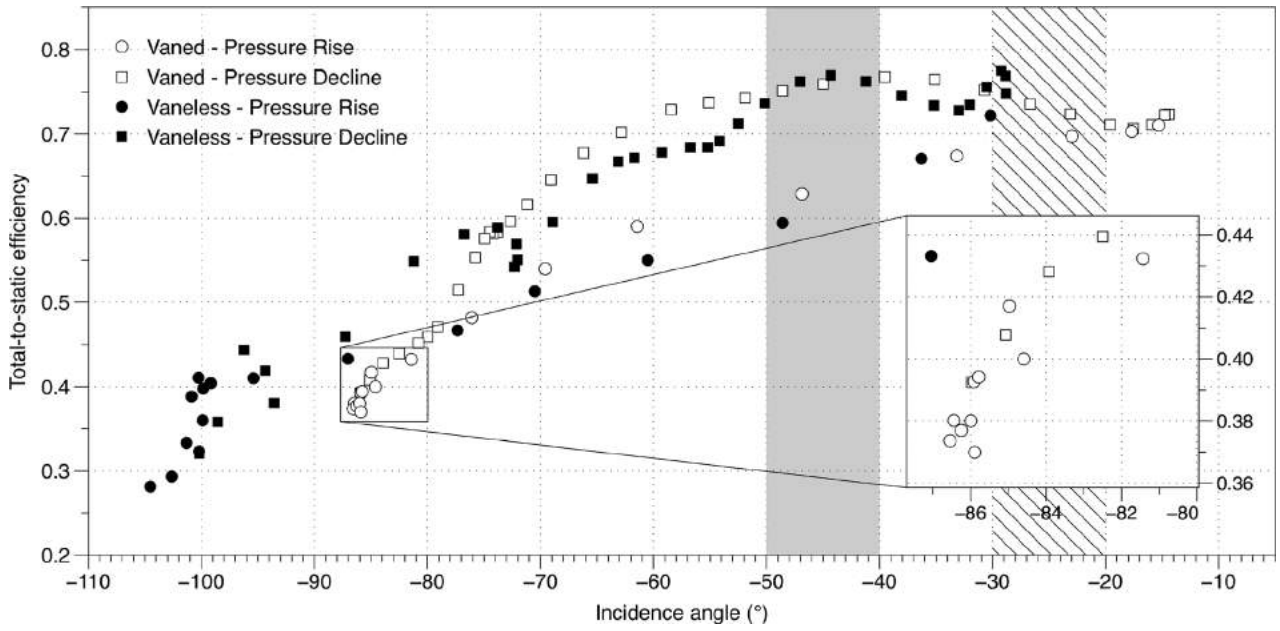

Fig. 11 Plot of instantaneous efficiency against incidence angle for vaned and vaneless turbine arrangement

during pressure decline period. The plot of instantaneous efficiency against incidence angle formed a counter-clockwise hysteresis loop with the maximum efficiency for both turbine arrangements occur during pressure decline. The plot in Fig. 11 indicates a wide range of incidence angle, which is 62 deg for vaned turbine and 77 deg for vaneless turbine. This condition is unfavorable for any turbomachine to work on as they are only capable of operating in a narrow range of incidence angle (within 10 deg). It can also be seen that, during the pressure decline period, the maximum efficiency corresponds to incidence angle with the range between −50 deg and −40 deg (shaded area in Fig. 11). This observation contradicts the classical turbo machinery theory, which indicated that maximum efficiency should occur when the incidence angle is in the range between −30 deg and −20 deg (indicated with stripes in Fig. 11). Figure 11 also indicates that the incidence angle range for the vaneless turbine has shifted toward more negative values. This is possibly due to the lack of low momentum flow guidance, as the interspace between volute exit and rotor inlet for the vaneless turbine is relatively large.

It is also noticed from Fig. 11 that the instantaneous efficiency points tend to be accumulated at either the highest or the lowest end of incidence angle plot. An example of this accumulation is indicated in a box in Fig. 11. When this box is magnified, it is clear that the collection of points are comprised of instantaneous efficiency points for both pressure rise and pressure decline period. This behavior indicated that majority of the vaned turbine operations are at either the highest, or the lowest pressure. Meanwhile, for the vaneless turbine, it can be seen that the instantaneous operating points are distributed more evenly throughout the incidence angle range.

Furthermore, while the efficiency hysteresis loop for vaned turbine is easy to trace, it is rather difficult to observe any trend that exists for the vaneless turbine efficiency plot. It is possible that this difficulty is the result of complex flow mixing that occurs close to the tongue due to flow recirculation in the vaneless turbine. The wake of this mixing propagates through the volute circumference and tends to have large effect on the vaneless turbine as the rotor leading edge is completely exposed to the volute exit. This feature could alter the incidence angle as the wake flow could result in changes of the absolute flow angle. Changes in this particular parameter inevitably alter the shape of the instantaneous velocity triangle, which, in turn, alter the incidence flow angle. Perhaps, this phenomenon is best studied by investigating the absolute flow angle that leaves the volute and flows into the rotor inlet.

Figure 12 shows the plot of absolute flow angle at volute exit and rotor inlet against the phase angle. The plot for vaned turbine is indicated with thinner line while vaneless turbine is represented by thicker lines. At the volute exit, it can be seen that the vaned turbine is able to maintain a constant flow angle of 67 deg throughout the pulse cycle. Meanwhile, the flow angle for vaneless turbine fluctuates with the range of ±6 deg between 60 deg and 66 deg. There is no clear trend that can be seen from this fluctuation. This observation indicates that the geometry downstream the volute exit (with or without vanes) could influence the flow condition upstream. In the vaneless turbine, the flow seems to turn radially inward at a larger radial location as compared to the vaned turbine. This results in lower averaged absolute flow angle at the turbine exit for vaneless turbine. Furthermore, the fluctuations that exist for vaneless turbine plot are potentially due to the wake flow that originated from the volute tongue, and also due to the large flow mixing areas of the flow recirculating from the volute end to the primary flow entrance.

Close to the rotor inlet, by assuming free vortex conditions, it is expected that the absolute flow angle would be increased uniformly. However, this is not the case for both the turbine configurations. For vaned turbine, Fig. 12 indicates that the absolute flow angle has dropped to 64 deg at phase angle between 0 deg and 60 deg. Afterward, at the instance of more than 60 deg, the flow angle exceeded that at volute exit to 70 deg. The uncertain trend of absolute flow angle, close to the rotor inlet, even with the addition of vane rows shows the complexity of flow behavior within the turbocharger turbine stage. Meanwhile, the behavior of absolute flow angle for vaneless seems to offset its vaned counterpart by 7 deg lower. However, this behavior is only valid until the phase angle of 240 deg before fluctuation occurs until the end of the pulse cycle. As with the case of volute exit, there is no clear trend of flow angle fluctuation at rotor inlet in vaneless turbine configuration.

Figure 13(*a*) shows the contour of absolute flow angle distribution within vaned and vaneless turbine during an instance of pressure rise period. For the purpose of this analysis, contour of absolute flow angle at phase angle of 72 deg is selected where

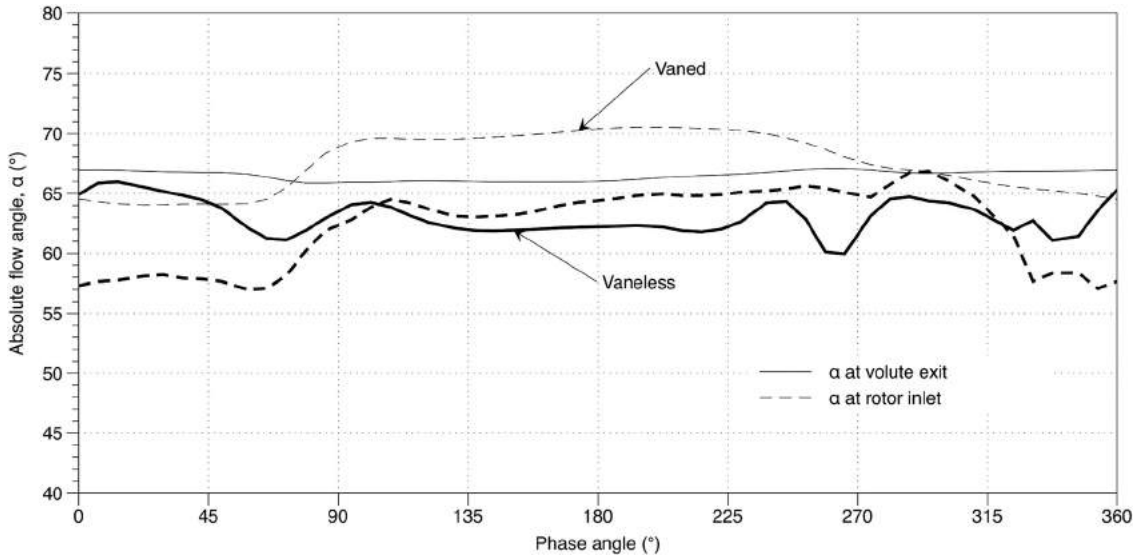

Fig. 12 Plot of absolute flow angle at volute exit and rotor inlet for vaned and vaneless turbine configuration

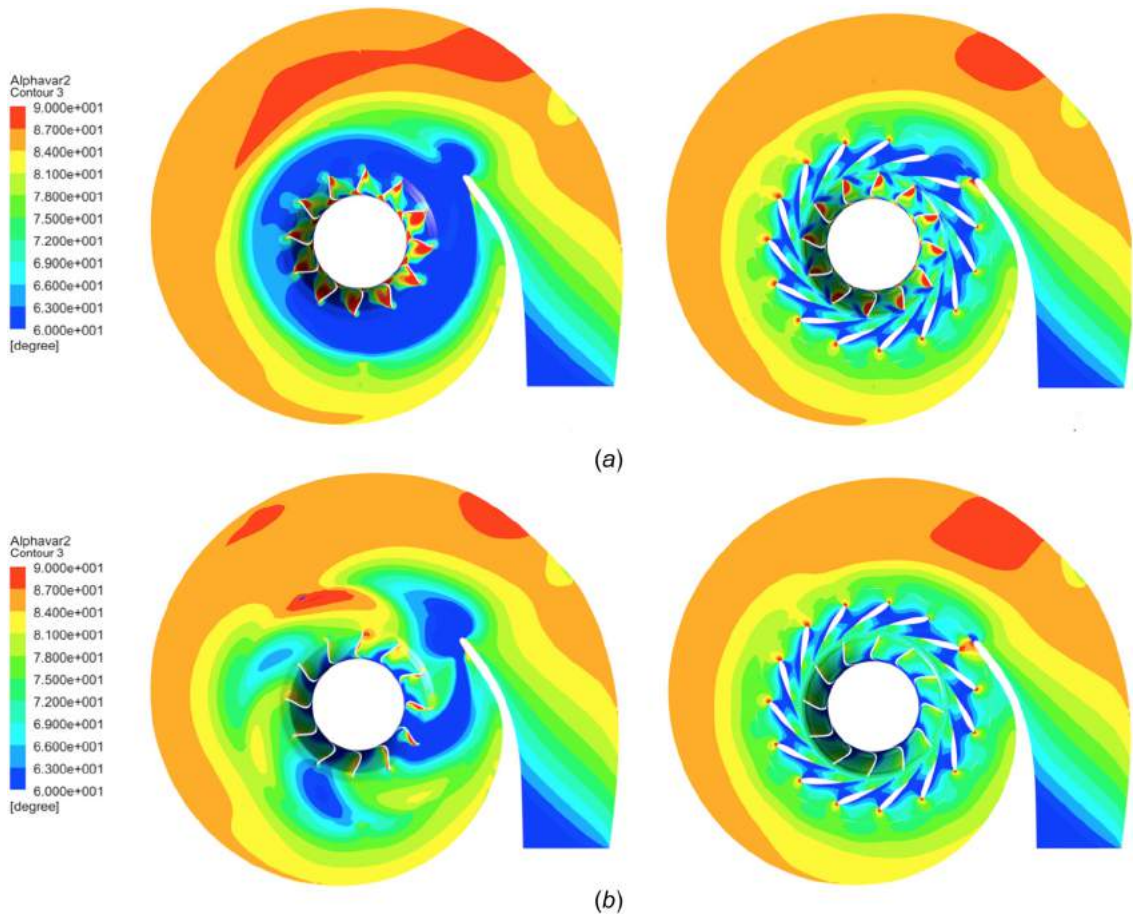

Fig. 13 The plot of instantaneous absolute flow angle for vaned and vaneless volute during (*a*) pressure rise instance and (*b*) pressure decline instance

Fig. 12 indicated that on average, the vaneless flow angle is 10 deg lower than its vaned counterpart at the volute exit and the rotor inlet. From Fig. 13(*a*), it can be seen that for both turbine arrangements, the flow angle tends to decrease as the flow travels into the rotor. However, for vaned turbine, even though it is clear that the flow angle starts to decrease downstream the volute exit and into the vane stage, its value seems to have increased again due to flow alignment in the vane passages. This results in the flow entering the vaned turbine at higher flow angle as compared to the vaneless turbine. In the latter case, there is nothing upstream

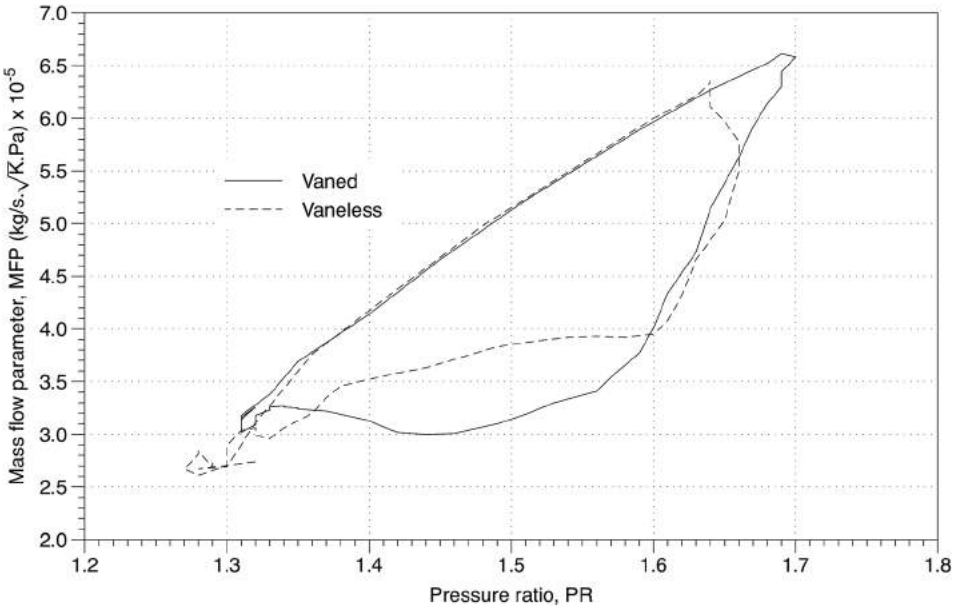

Fig. 14 Plot of instantaneous mass flow parameter against pressure ratio for vaned and vaneless turbine arrangements

the rotor inlet to prevent the flow angle from keeping it decreased before entering the rotor inlet. Furthermore, close to the tongue, there is a region of low flow angle for both the turbine arrangements, which is most probably due to mixing that occurs when the flow at the end of the volute circumference recirculates back into the main volute passage. For vaned turbine, this region of low flow angle has migrated well into the vane passage that is located at the proximity of the tongue.

While there is a certain degree of similarity that occurs on the flow angle distribution between vaned and vaneless turbine during pressure rise period, none occur during pressure decline period, specifically at the phase angle of 230 deg, as indicated in Fig. 13(*b*). The vaneless turbine indicated massive distortion on the distribution of flow angle where large region of low flow angle can be seen close to the tongue, and further downstream into the rotor inlet. The flow angle also does not maintain a constant value in circumferential direction at the rotor inlet. These distortions would ultimately result in uneven incidence angle distribution, which forces the turbine to operate outside its envelop of optimum incidence angle. Meanwhile, for the vaned turbine, the flow angle is distributed uniformly, with only a small region of low flow angle close to the volute tongue.

3.2.2 Differences in Swallowing Capacity. Figure 14 shows the plot of the instantaneous mass flow parameter against pressure ratio for both turbine arrangements. Both turbines show clockwise hysteresis loop for their swallowing capacity. In general, it is obvious that the hysteresis mass flow parameter loop for the vaneless turbine is shifted toward lower values of mass flow parameter and pressure ratio as compared to its vaned counterpart. This behavior could be attributed to lower flow blockage due to the absence of guide vanes, which results in lower magnitude of mass flow accumulation as compared to the vaned turbine. Meanwhile, the vaned turbine indicated higher magnitude of maximum mass flow parameter and pressure ratio due to the flow blockage at the vane rows. For both configurations, during the pressure rise period, the mass flow parameter rises together almost linearly with the pressure ratio. However, the relationship is no longer linear during pressure decline period where the mass flow parameter drops at higher rate compared to pressure ratio.

Another interesting observation from Fig. 14 is that for the vaned turbine, the mass flow parameter and pressure ratio achieved their peak at the same instance. Meanwhile, for the vaneless turbine, the mass flow parameter achieved its peak slightly earlier than the pressure ratio. This observation indicated strong presence of pressure reflection that occurs only in the vaneless turbine. The pressure wave reflected on the turbine wheel could travel back to the volute inlet, and with the absence of the vane blades, the reflected wave that arrives at the volute inlet will have a large magnitude. The lack of pressure reflection for vaned turbine also suggested that the vane blades could act as a damper, thus minimizing the effect of pressure reflection.

Another major difference between the two turbine arrangement is seen during pressure decline period between $PR = 1.37$ and $PR = 1.60$. At this particular range of pressure ratio, it can be seen that vaneless turbine indicated slower rate of mass flow decline as compared to its vaned counterpart. This feature could be attributed to accumulation of mass at the volute inlet. It is possible that the exposed turbine wheel in the vaneless turbine has resulted in excitation of centrifugal effect, which in turn promotes mass accumulation at the turbine inlet shortly after the peak of each of the pulses. This feature contradicts the observation made during pressure rise where the mass flow in the vaned turbine tends to accumulate due to the blockage effect introduced by the vane blades.

3.2.3 Comparison of Static Pressure Distribution Within the Turbine Stage. This section discusses the comparison of pressure traces within the turbine stage between the two stator arrangements. For the first analysis, the pressure at three locations along the volute circumference, namely at 60 deg, 180 deg, and 240 deg, is extracted and analyzed in order to evaluate its propagation with respect to time. These locations are shown in Fig. 15. Second analysis involves the measurement of static pressure at a constant volute angle of 180 deg, but at different radial locations which are the volute centroid, the volute exit, and the rotor inlet, also with respect to time.

Figure 16 shows the instantaneous static pressure trace at 60 deg, 180 deg and 240 deg of volute circumference for both stator configurations. At 60 deg volute centroid and during pressure the rise until the peak, the pressure trace between the two volutes shows similar behavior. However, at the beginning of pressure decline ($\emptyset = 112$ deg), the vaneless turbine has indicated sharper pressure reduction as compared with the vaned turbine. However, at $\emptyset = 180$ deg, results indicated that the pressure for vaneless

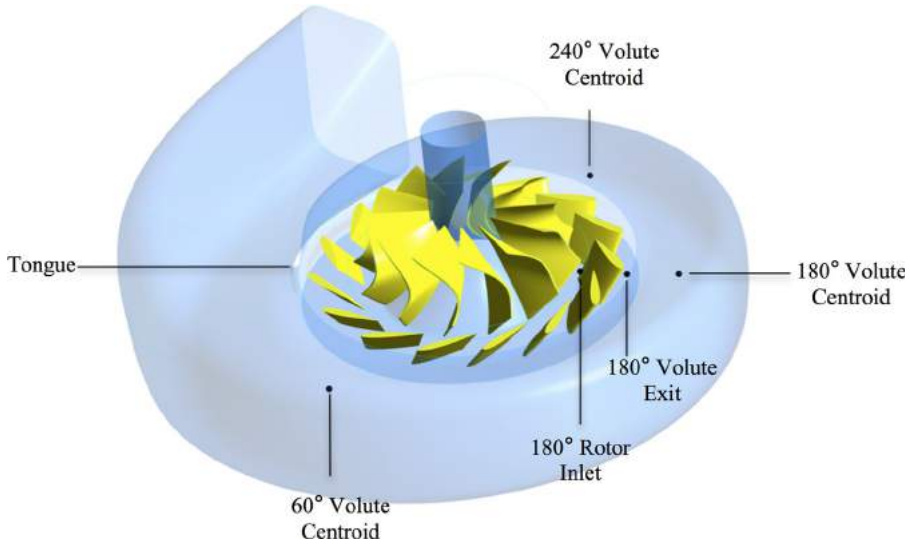

Fig. 15 Measurement locations within the computational domain

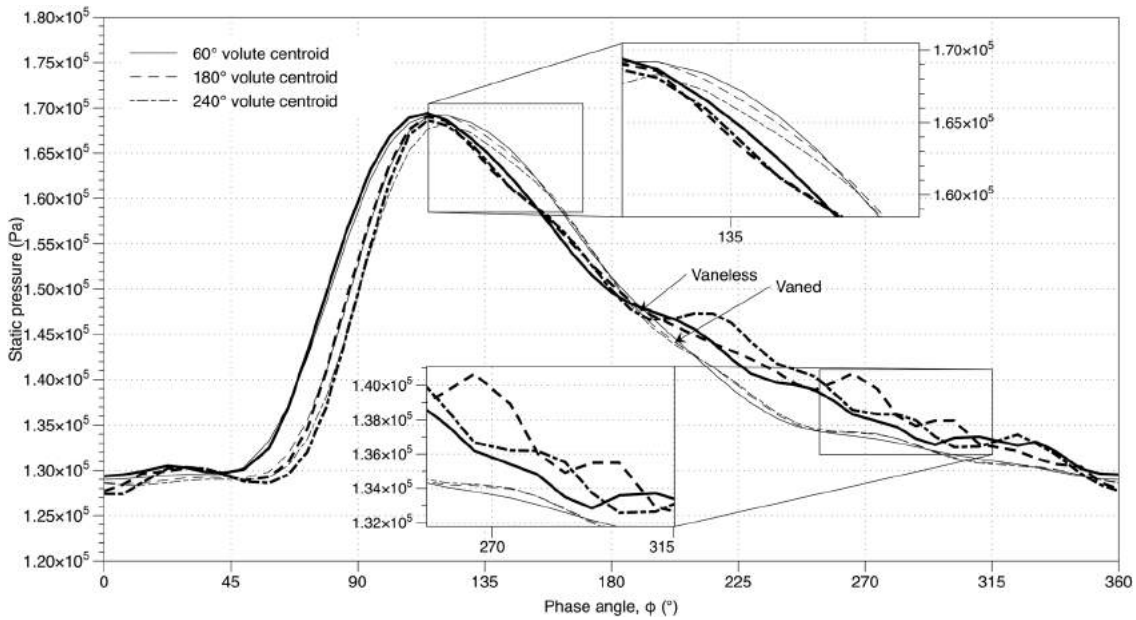

Fig. 16 Instantaneous static pressure trace at 60 deg, 180 deg and 240 deg of volute centroid for both vaned and vaneless configuration

turbine exceeded that of vaned turbine as a result of slower rate of pressure decline. The behavior of rapid drop in pressure for vaneless turbine at the beginning of pressure decline period is attributed to the unblocked pressure propagation into the turbine wheel. Meanwhile, for the vaned turbine, the existence of the nozzle rows has introduced additional surfaces for pressure reflection. This is translated into less degree of pressure reduction at 60 deg volute circumference. Furthermore, at $\emptyset = 240$ deg, it can be seen that the magnitude of static pressure for vaneless turbine has started to show minor fluctuations until the end of the pulse cycle. On the contrary, for the vaned turbine, smooth trend of pressure decline is seen until $\emptyset = 360$ deg.

At 180 deg volute location, the clear phase shift from the 60 deg pressure trace could clearly be seen during pressure rise period. This behavior is expected as pressure travels through the volute section at finite time. The pressure profile trend for the vaneless turbine after the peak is similar to the trace at the 60 deg location, but only until $\emptyset = 190$ deg. Close to the end of the pulse cycle, the pressure profile has started to show fluctuations that are at the amplitude higher than the fluctuations recorded at the 60 deg volute location. Meanwhile, the vaned turbine seems to be able to maintain a smooth curvature of pressure decline, identical to that at 60 deg volute circumference. These fluctuations probably occur due to lack of flow guidance in the absence of guide vanes. It is also possible that this condition is the direct effect of the pressure pulse hitting the rotating rotor in vaneless turbine, thus resulting in localized fluctuations in pressure magnitude in the volute. As compared to the vaned turbine, the pressure only interacts with stationary stator, which in turn indicated more stable behavior.

The comparison between pressure profile at 240 deg location of the volute between vaned and vaneless turbine is also shown in Fig. 16. It can be seen that the magnitude of the instantaneous static pressure still remains the same between vaned and vaneless turbine during pressure rise period. However, there are slight

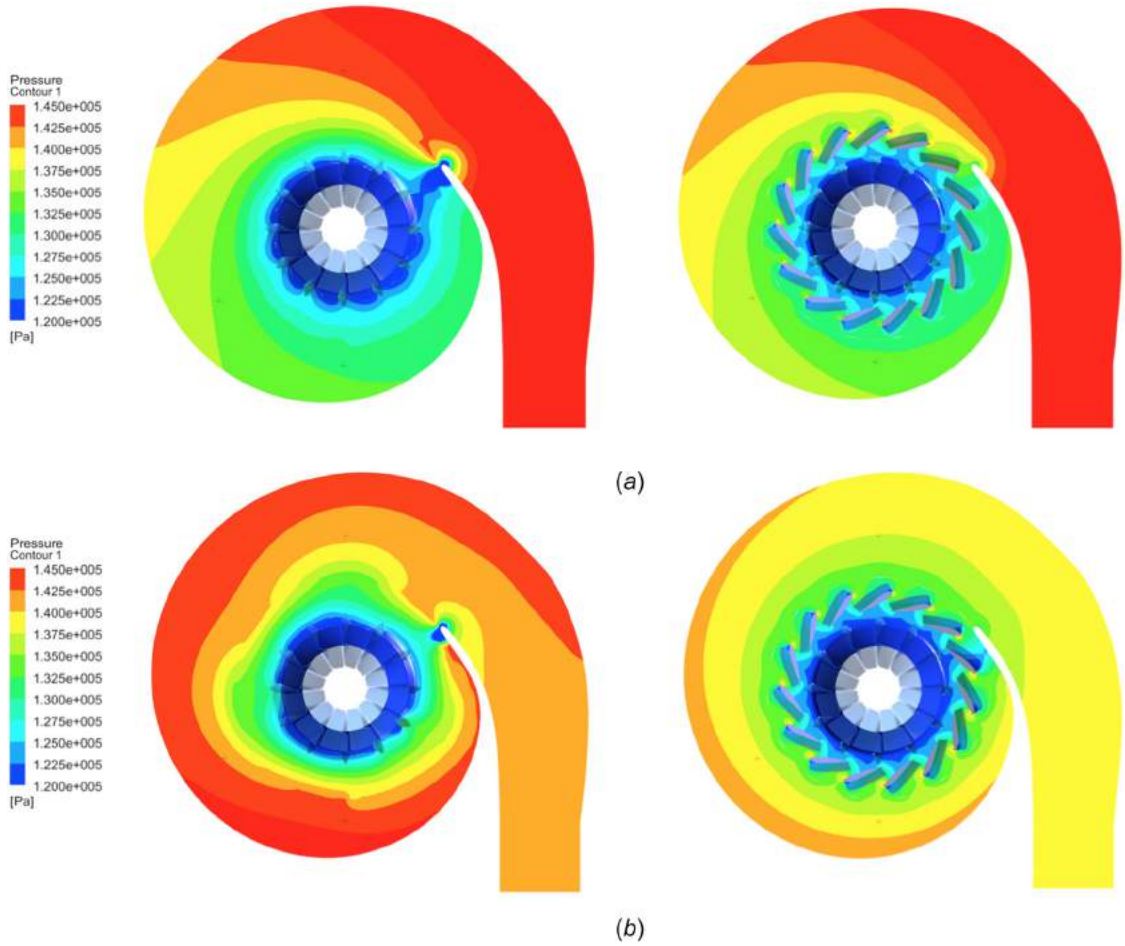

Fig. 17 The contour plot of instantaneous static pressure distribution within the vaned and vaneless volute during (*a*) pressure rise instance and (*b*) pressure decline instance

differences in the pressure trace at the start of pressure decline period until $\emptyset = 190$ deg. At later phase angle than $\emptyset = 190$ deg, the pressure fluctuations that were observed in vaneless turbine at volute circumference of 60 deg and 180 deg could be seen, but with the higher amplitude of fluctuations. This is an obvious indication that not only the vaneless turbine is exposed to back pressure from the rotating component, it is also worsening as the flow gets closer to the volute tongue before entering recirculation region. This observation suggests that the pressure reflection originated close to the end of volute circumference. This condition is not favorable to primary flow and also increases the possibility of reversed flow close to the tongue as indicated by Padzillah et al. [11]. Again, as indicated earlier, the pressure trace in the vaned volute is still able to maintain smooth and similar profile to that upstream volute location. The difference between the pressure trace of the vaned and vaneless volute that increases as the flow travels downstream the volute circumference suggests that the vaneless volute is subject to a completely different gas dynamics behavior than the vaned volute especially during pressure decline. The empty space that exists between volute exit and turbine entry for vaneless turbine allows for smooth travel of pressure wave reflections and its superposition.

In order to further evaluate the differences in flow phenomena at 60 deg, 180 deg, and 240 deg volute circumference between vaned and vaneless turbine, two instances during pressure rise and pressure decline are selected for flow field analysis, shown in Fig. 17. During pressure rise, it can be seen in Fig. 16 that the pressure trace at different locations indicated similar trends and magnitudes. For this purpose, 70 deg phase angle has been selected for analysis where the pressure distribution between the two turbine arrangements is shown in Fig. 17(*a*). The volute centroid location where the measurement for 60 deg, 180 deg, and 240 deg are marked in Fig. 15. In general, it can be seen that the flow field within the volute maintains its similarity between the two turbines until the end of volute circumference. There is, however, a significant difference close to the volute tongue where the vaneless volute indicated a region where massive pressure drop occurs and extends from the tongue into the rotor inlet. Meanwhile, for the vaned turbine, the pressure distribution at the tongue also experience pressure drop but is relatively small as compared to its vaneless counterpart.

During the pressure decline, plot in Fig. 16 indicated that the pressure trace between the vaned and vaneless volute is no longer identical. Therefore, the phase angle of 230 deg is selected for further analysis. The comparison of pressure contour within the turbine stage at $\emptyset = 230$ deg is shown in Fig. 17(*b*). The distribution in vaned turbine seems to be more uniform when compared to the vaneless turbine. In the vaneless turbine, there seem to be high level of pressure reflection that results in uneven radial pressure distribution. The range of pressure distribution at this instance is also larger for vaneless turbine compared to its vaned counterpart. This unpredictable behavior also occurs during other instances of pressure decline period. Therefore, a trend of pressure fluctuations in the vaneless volute, away from pressure trace for vaned turbine at volute centroid for 60 deg, 180 deg, and 240 deg circumferences during pressure decline, could be seen in Fig. 16.

Figure 18 shows the static pressure trace of vaned and vaneless turbine configurations at 180 deg circumference location against

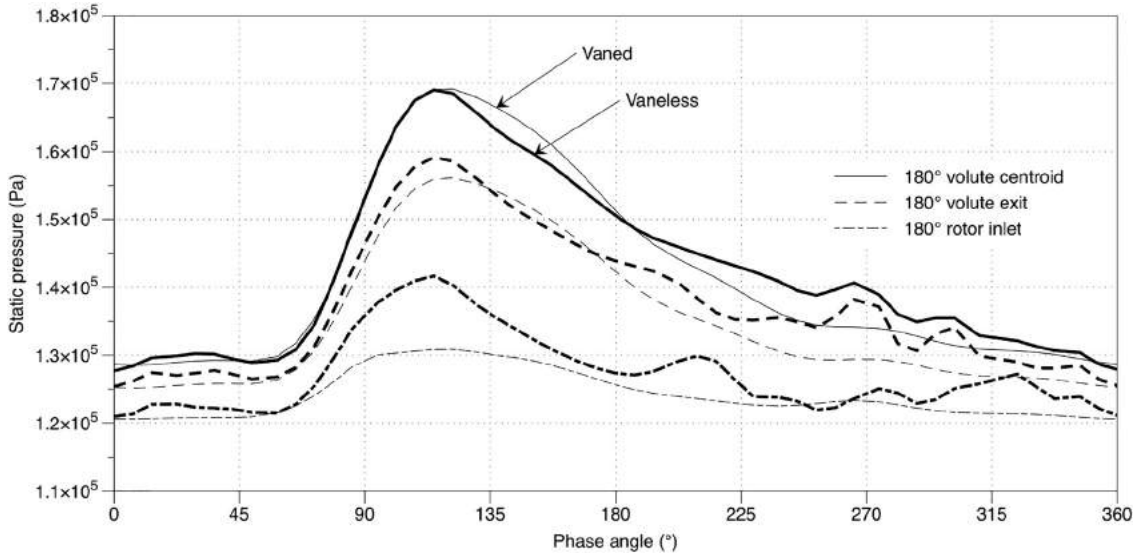

Fig. 18 The plot of instantaneous static pressure trace at 180 deg volute centroid, volute exit, and rotor inlet

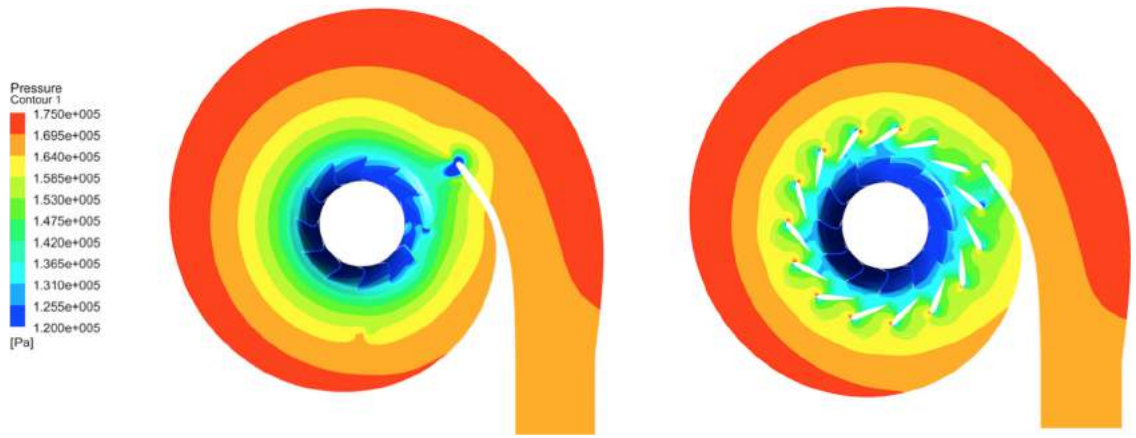

Fig. 19 The plot of instantaneous static pressure contour at the peak cycle pressure

the pulse phase angle. At the particular circumferential location, three locations have been selected for extraction of the magnitude of static pressure, namely the volute centroid, volute exit, and rotor inlet. The measurement locations are visualized in detail in Fig. 15. The thinner line in Fig. 18 shows the pressure trace for the vaned turbine while a slightly thicker line is used to represent the pressure trace for the vaneless turbine. During the pressure rise period, the pressure trace at the volute centroid for both the turbine arrangements indicates identical behavior in both trend and magnitudes. However, as soon as the pressure starts to decline, the vaneless turbine shows slower pressure decline rate as compared to the vaned turbine. Close to the end of the pulse cycle, it can be seen that there are multiple fluctuations that emerge for the vaneless turbine, indicating the strong presence of pressure reflection and superposition.

As the flow travels radially downstream at the volute exit, the pressure trace during the pressure rise period between the two configurations is no longer identical. It can be seen that pressure rises more rapidly for vaneless turbine and achieves a slightly larger peak as compared to the vaned turbine. Despite that, the peak pressure still occurs at similar instance of the phase angle. After the peak, the vaned turbine shows gradual and smooth decline of pressure until the end of the pulse cycle. On the contrary, the pressure trace at the volute exit of the vaneless turbine after its peak shows unpredictable rising and declining trends, and also shows multiple peaks at $\emptyset = 270$ deg and $\emptyset = 300$ deg. This behavior is attributed to uneven pressure propagation due to the mixing that occurs at recirculation region near the tongue, as well as the pressure wave that is reflected off the rotating turbine wheel surfaces. The vaned turbine does not show such feature as the mixing that occurs at the recirculation region is minimal. The existence of the guide vanes also acts as a "damper" to the reflected pressure wave from the turbine wheel blade surface, as previously explained.

The behavior of smooth rising and declining pressure for the vaned turbine holds true even at the position close to the rotor inlet. However, for its vaneless counterpart, the deviations start as early as $\emptyset = 50$ deg. During the pressure rise period, it can be seen that the pressure rises rapidly for the vaneless turbine. At its peak, the magnitude recorded is twice than the peak pressure recorded for the vaned turbine, despite similar phase angle instance. This feature highlights the difficulties in pulsating flow turbine research as it indicates large magnitude of pressure reflection and superposition until the end of the pulse cycle. Thus, the operating condition of the turbine wheel would be far away from its intended steady-state design conditions.

Figure 19 shows the contour of pressure distribution within the vaned and vaneless turbine at peak pressure, which occurs at the phase angle of 108 deg. For the vaneless volute, a small region of low pressure is shown close to the tongue. At this instance, the

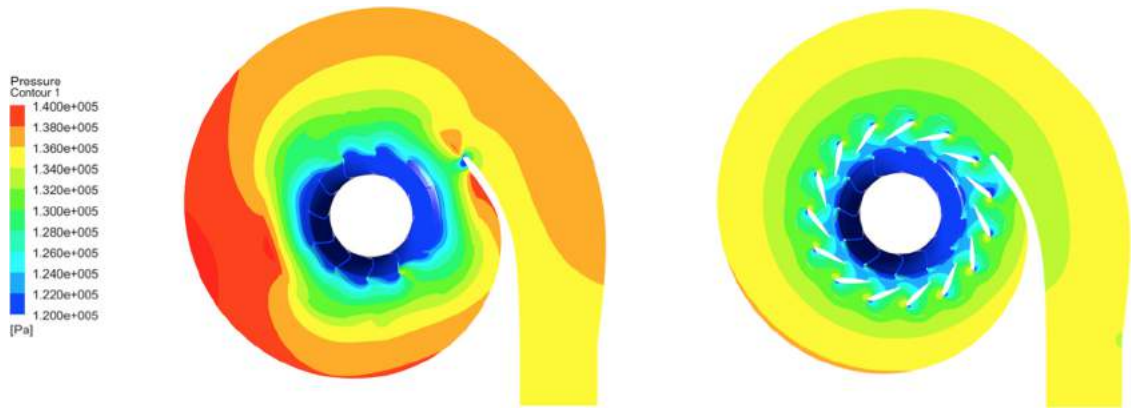

Fig. 20 The plot of instantaneous static pressure distribution at $\emptyset = 274$ deg

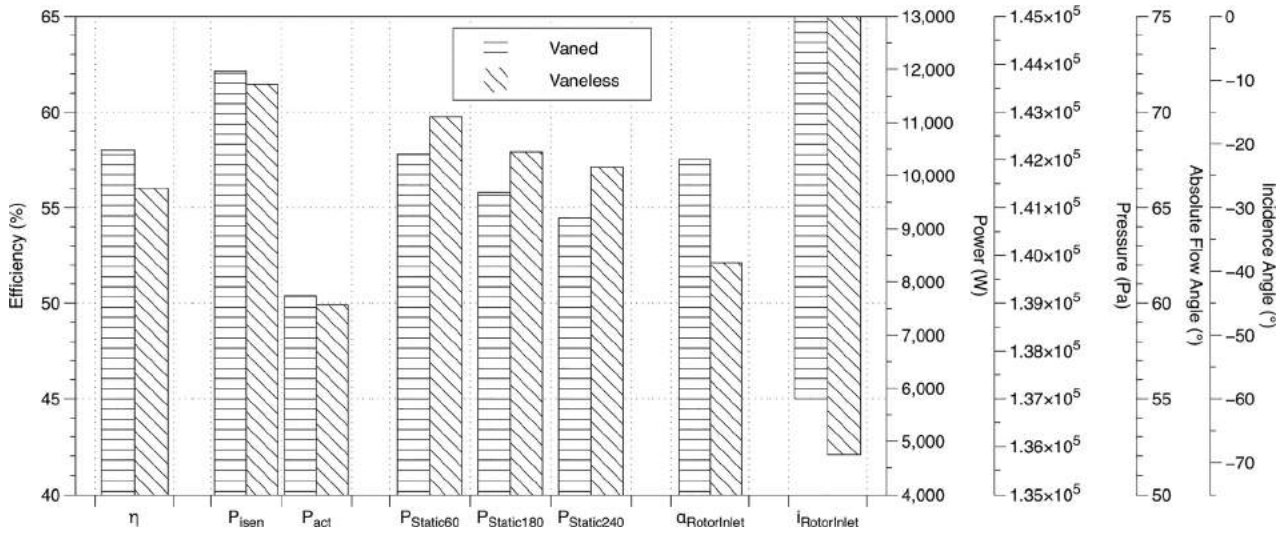

Fig. 21 Comparison of averaged parameters for vaned and vaneless volute arrangements

measured static pressure at 180 deg volute circumference for both turbine arrangements indicates a similar magnitude as shown in Fig. 18 earlier. As the flow travels radially inward to the volute exit, the pressure drops at a faster rate in the vaned volute as compared to its vaneless counterpart. The pressure contours in Fig. 19 show that in the vaned volute, the existence of the vane blades has resulted in the formation of low pressure region on the blade suction side and that this low pressure region influenced the flow field at the volute exit through back pressure. Meanwhile, in the vaneless volute, the pressure drop as the flow moves radially inward seems to be uniformly distributed throughout the circumference. As the flow travels to the turbine inlet, it is clear that for the vaned turbine, the flow has accelerated, resulting in much lower pressure trace as compared to the vaneless turbine. However, this feature is only true during the peak of each of the cycles. During the pressure decline period, the difference in the pressure trace between the vaned and vaneless volute is less aggressive, indicating that the vane blades are not capable of accelerating the low momentum flows.

In order to investigate in greater detail about this phenomena, a contour of pressure distribution at $\emptyset = 274$ deg is plotted as shown in Fig. 20. It was indicated earlier in Fig. 16 that the pressure is fluctuating heavily at this instance for the vaneless turbine. This phenomenon is captured clearly in the pressure contour distribution where the comparison between the two volute arrangements indicated massive differences. While the vaned volute maintains the radially uniform pressure drop across the circumference, the vaneless volute shows evidence of pressure reflection, thus unable to maintain its uniform distribution as seen earlier during the peak of the pulse. Therefore, the characterization of the flow phenomena within the vaneless volute is more challenging than that of the vaned volute.

Figure 21 shows the comparison of the averaged values of a few parameters investigated in this work between vaned and vaneless volute. The bar for the vaned volute is indicated by horizontal stripes while the vaneless volute is indicated by diagonal stripes. It can be seen that the cycle-averaged efficiency for both volutes is significantly lower than during the steady-state operation (indicated in Fig. 8). The cycle-averaged efficiency for the vaned volute is found to be 2.5 points higher than its vaneless counterpart. This could be attributed to the magnitude of averaged incidence angle for vaned turbine, which is closer to the indicated optimum range between −40 deg and −50 deg as compared to the vaneless turbine. The magnitudes for the isentropic and actual power are also higher for the vaned turbine, despite they are subject to similar pressure profile at inlet. However, the averaged static pressure traces indicated different behavior where they indicated higher magnitude for the vaneless volute as compared to the vaned volute at 60 deg, 180 deg, and 240 deg centroid of the volute circumference as compared to its vaned counterpart. This behavior indicates the existence of large magnitude of pressure reflection in the vaneless volute during pressure decline period as

the turbine wheel is directly exposed to the volute. This in turn results in higher averaged magnitude of static pressure in the particular arrangement. Finally, the comparison of averaged flow angle at the rotor inlet shows that the flow angle is 8 deg higher in the vaned volute as compared to the vaned volute. This feature has been explained in greater detail in Fig. 12.

This investigation has revealed several interesting observations at the flow field level, which ultimately results in the performance differences between the vaned and vaneless volute. The integration of the results obtained from this research with turbine selection and matching procedures could potentially help engine designers in the selection of either vaned or vaneless turbine to be used.

4 Conclusion

This work presented the differences in flow field behavior between vaned and vaneless volutes and its effects on the turbocharger turbine performance under pulsating flow condition. This is achieved by the development of a fully validated three-dimensional CFD turbocharger turbine model. The analysis of the relationship between the incidence angle and instantaneous efficiency revealed that the maximum efficiency could be achieved with the incidence angle range between −40 deg and −50 deg for both vaned and vaneless volute. This range is far from the classical theory that indicates the optimum incidence angle range between −20 deg and −30 deg. Furthermore, the hysteresis loop that is formed by vaned volute seems to be more uniform as compared to the vaneless volute. A closer look into the absolute flow angle distribution for the two arrangements showed that the flow tends to turn radially inward at higher radial location in vaneless turbine than its vaned counterpart. This ultimately results in lower absolute flow angle for the vaneless turbine. Moreover, the additional flow angle fluctuations detected near the end of the pulse cycle resulted in a nonuniform efficiency against incidence angle hysteresis loop for the vaneless turbine.

For the comparison of swallowing capacity behavior between the two turbine arrangements, it was shown that during pressure rise, vaned turbine would accumulate mass at the inlet due to the flow blockage from the existence of the vane blades. Meanwhile, during pressure decline period, vaneless turbine would accumulate more mass due to strong centrifugal effect from the turbine wheel. The analysis on pressure propagation along the volute circumference indicated an increasingly higher pressure reflection and superposition as the flow reaches the end of the volute for the vaneless turbine, which suggests that the strongest pressure reflection occurs at the end of the volute. This behavior does not seem to exist for the vaned volute. A closer look at the flow propagation at 180 deg circumference location revealed that the vaneless turbine suffers an increasing magnitude of pressure fluctuation as the flow gets closer to the rotor. Meanwhile, the vaned volute is able to maintain smooth pressure rise and decline regardless of the radial location, thus indicating the averaged efficiency that is 2.5 points higher than the vaneless volute. It could also be concluded from this work that the vaneless turbine flow field distribution is more sensitive toward the incoming pulsating flow, resulting in uneven pressure and velocity contour especially during pressure decline period, as compared to its vaned counterpart.

Funding Data

- Ministry of Higher Education, Malaysia (Grant No. R.J130000.7824.4F83).

Nomenclature

C = isentropic velocity (m/s)
I = moment of inertia (kg/m^2)
$\dot{m}$ = mass flow rate (kg/s)
N = rotational Speed (rpm)
P = pressure (Pa)
t = time (s)
T = temperature (K)
U = velocity (m/s)
ν = kinematic viscosity (m^2/s)
ρ = density (kg/m^3)
τ = torque (N·m)
$\emptyset$ = phase angle (deg)

Subscripts

act = actual
exp = experiment
Isen, is = isentropic
sim = simulation
01 = inlet
5 = exit

References

[1] Baines, N. C., and Lavy, M., 1990, "Flows in Vaned and Vaneless Stators of Radial-Inflow Turbocharger Turbines," International Conference on Turbochargers and Turbocharging, London, May 22–24, pp. 7–12.
[2] Spence, S. W., Rosborough, R. S., Artt, D., and McCullogh, G., 2007, "A Direct Performance Comparison of Vaned and Vaneless Stators for Radial Turbines," ASME J. Turbomach., **129**(1), pp. 53–61.
[3] Karamanis, N., Palfreyman, D., Arcoumanis, C., and Martinez-Botas, R. F., 2006, "Steady and Unsteady Velocity Measurements in a Small Turbocharger Turbine With Computational Validation," J. Phys. Conf. Ser., **45**(1), pp. 173–173.
[4] Yang, M. Y., Padzillah, M. H., Zhuge, W. L., Martinez Botas, R. F., and Rajoo, S., 2014, "Comparison of the Influence of Unsteadiness Between Nozzled and Nozzleless Mixed Flow Turbocharger Turbine," 11th International Conference on Turbochargers and Turbocharging, London, May 13–14, pp. 333–345.
[5] Lam, J.-W., Roberts, Q. D. H., and McDonnel, G. T., 2002, "Flow Modelling of a Turbocharger Turbine Under Pulsating Flow," Seventh International Conference on Turbochargers Turbocharging, London, May 14–15, pp. 181–197.
[6] Palfreyman, D., and Martinez-Botas, R. F., 2005, "The Pulsating Flow Field in a Mixed Flow Turbocharger Turbine: An Experimental and Computational Study," ASME J. Turbomach., **127**(1), pp. 144–155.
[7] Karamanis, N., Martinez-Botas, R. F., and Su, C. C., 2001, "Mixed Flow Turbines: Inlet and Exit Flow Under Steady and Pulsating Conditions," ASME J. Turbomach., **123**(2), pp. 359–371.
[8] Copeland, C. D., Newton, P., Martinez-Botas, R. F., and Seiler, M., 2012, "A Comparison of Timescales Within a Pulsed Flow Turbocharger Turbine," Tenth International Conference on Turbochargers and Turbocharging, London, May 15–16, pp. 389–404.
[9] Newton, P., Martinez-Botas, R., and Seiler, M., 2014, "A Three-Dimensional Computational Study of Pulsating Flow Inside a Double Entry Turbine," ASME J. Turbomach., **137**(3), p. 031001.
[10] Greitzer, E. M., Tan, C. S., and Graf, M. B., 2004, *Internal Flow, Concepts and Applications*, Cambridge University Press, Cambridge, UK.
[11] Padzillah, M. H., Yang, M., Zhuge, W., and Martinez-Botas, R. F., 2014, "Numerical and Experimental Investigation of Pulsating Flow Effect on a Nozzled and Nozzleless Mixed Flow Turbine for an Automotive Turbocharger," ASME Paper No. GT2014-26152.
[12] Dale, A., and Watson, N., 1986, "Vaneless Radial Turbocharger Turbine Performance," Third International Conference on Turbocharging and Turbochargers, London, May 6–8, pp. 65–76.
[13] Rajoo, S., 2007, "Steady and Pulsating Performance of a Variable Geometry Mixed Flow Turbocharger Turbine," Ph.D. thesis, Imperial College of Science, Technology and Medicine, London.
[14] Szymko, S., 2006, "The Development of an Eddy Current Dynamometer for Evaluation of Steady and Pulsating Turbocharger Turbine Performance," Ph.D. thesis, Imperial College of Science, Technology and Medicine, London.
[15] Pesiridis, A., and Martinez-Botas, R., 2005, "Experimental Evaluation of Active Flow Control Mixed-Flow Turbine for Automotive Turbocharger Application," ASME Paper No. GT2005-68830.
[16] Chiong, M. S., Rajoo, S., Romagnoli, A., Costall, A. W., and Martinez-Botas, R. F., 2014, "Integration of Meanline and One-Dimensional Methods for Prediction of Pulsating Performance of a Turbocharger Turbine," Energy Convers. Manage., **81**, pp. 270–281.
[17] Padzillah, M. H., Rajoo, S., Yang, M., and Martinez-Botas, R. F., 2015, "Influence of Pulsating Flow Frequencies Towards the Flow Angle Distributions of an Automotive Turbocharger Mixed-Flow Turbine," Energy Convers. Manage., **98**, pp. 449–462.